BOUNDARY INTEGRAL METHODS FOR CAVITATION BUBBLES NEAR BOUNDARIES

J. R. Blake, A. Pearson and S. R. Otto

The University of Birmingham,
Edgbaston, Birmingham B15 2TT, United Kingdom

Abstract

The paper will review the art, craft and science of modelling cavitation bubbles near boundaries through the use of the boundary integral method. The presentation will come in four parts, namely, a discussion of recent experimental studies that have motivated our current research, understanding the physics associated with the phenomena, a detailed presentation on the boundary integral method and, finally, a detailed comparison between experiment and theory, indicating the improved understanding and interpretation of behaviour that the computed results provide.

1 Introduction

Much of the recent research has been associated with modelling the behaviour of laser generated bubbles near both rigid and very flexible boundaries. In the former case the study has been concerned with understanding the fluid mechanics associated with single cavitation bubble luminescence (SCBL). Because of the presence of the rigid boundary, the bubble collapses asymmetrically yielding a high speed liquid jet directed towards the boundary. For standoff distances below a critical value, the jet impacts against the other side of the bubble, leading to the formation of a toroidal bubble and a resulting ring vortex fluid motion. However, beyond the critical standoff, no jet impact occurs on the far side of the bubble with the bubble rebounding at a higher velocity than the jet. In SCBL studies, light does not appear to be emitted from the bubble until it reaches a critical distance from the boundary and thereafter light emission increases rapidly to the effectively infinite fluid result. Kinetic energy is associated with the ring vortex motion which is not available for compression and adiabatic heating of gas inside the bubble, thus leading to lower interior temperatures. The latter study near flexible surfaces is associated with modelling the behaviour of bubbles near tissue, or tissue phantoms. The research is of great importance to laser surgery and extracorporeal shock wave lithotripsy (ESWL). Observation and computation yield a vast array of results that require explanation.

In this paper a computational technique based on the boundary integral method is developed. The technique is well established for simply connected bubbles (see e.g. Guerri, Lucca & Prosperetti 1981, Blake, Taib & Doherty 1986,87) but needs significant adaptation for the doubly connected geometry of a toroidal bubble. Best (1993) overcame these difficulties by inserting a 'cut' across the jet penetrating the bubble in his earlier paper but later developed a dynamic cut relocation algorithm (Best 1994) that significantly improved the computational speed and accuracy.

The next section will discuss the background physics to the study, identifying key stages from the initiation of a laser generated bubble through to its collapse and later rebound. This shall be followed by the development of the computational technique for a simply and doubly connected bubble. Later examples will be shown for computer generated bubbles at: (i) a range of standoff distances from a rigid boundary, (ii) near a free surface and (iii) bubbles generated in a shallow liquid layer.

2 Background Physics - Laser Generated Bubbles

It is important to understand the background to the physics of laser-generated bubbles so that we may better understand the phenomena and to allow the development of realistic models, but also to be aware of

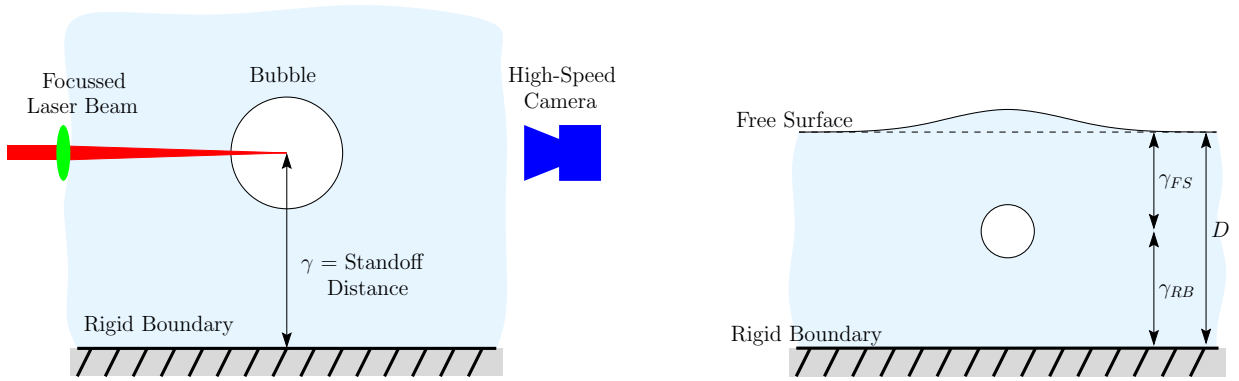

(a) Idealised schematic of the experimental set-up for SCBL.

(b) Shallow layer schematic

Figure 1: Schematic diagrams.

the limitations of the calculation. Mathematical modelling is after all only an approximation to nature but through modelling often a better understanding of phenomena can be obtained. In considering the behaviour of a laser-generated bubble near a boundary a number of stages can be clearly identified although the order in which they occur will depend on individual circumstances.

The first stage is the initiation stage associated with the firing of the laser which has a length measured in microseconds (μs). The laser generates a plasma in the liquid (usually water), leading to the dissociation of H_2O, the production of non-condensible gases, and from the fluid mechanics viewpoint, shock waves and high pressures, often as high as 1000 atmospheres or more. The next stage is associated with the bubble dynamics, and for the most part is relatively slow. Pressures are characterised by atmospheric pressure in most experiments so the velocity scale will be $O((p_a/\rho)^{1/2})$ where p_a is atmospheric pressure and ρ is the fluid density. For future reference this gives a characteristic velocity of about 10ms^{-1}, noting that $p_a \sim 10^5\text{Pa}$ and $\rho \sim 10^3\text{Kg m}^{-3}$. Thus $V \sim (p_a/\rho)^{1/2}$ is very much less than the speed of sound in water $c \sim 1500\text{ms}^{-1}$. For a typical mm-sized bubble this will give a Reynolds number of 10^{4-6} and an oscillation period T of $O(100\mu\text{s})$. The diffusion of vorticity timescale of a^2/ν yields O(10ms) which is very much larger than the bubble period. Thus around the laser-generated bubble beyond the first few μs it is reasonable to regard the fluid mechanics surrounding the bubble as being incompressible, inviscid and irrotational. This will remain a good approximation at least until jet impact or minimum volume for a non-spherical bubble. Thus the fluid velocity may be represented by the gradient of a potential function which satisfies Laplace's equation in the near-field surrounding the bubble. However, in the far-field the relevant equations should strictly be the wave equation (see Prosperetti & Lezzi 1986, Blake & Keen 1998).

As alluded to above, the next stage in the behaviour for a non-spherical bubble will either be liquid jet impact on the far-side of the bubble or minimum volume, depending on the physical circumstances associated with the generation of the bubble (see results later on the influence of standoff distance). Korobkin (1997) identifies five stages in jet impact. The first four stages consisting of supersonic, transonic, subsonic and inertial, no liquid flow is discernable as the timescale is $O(M^2D/V)$ where M is the Mach number, V, jet velocity and D jet diameter yielding a timescale of μs. Water hammer pressures of $O(\rho cV)$ will yield pressure of up to 1000 atmospheres but these will only prevail for a microsecond or less and are often not recorded on pressure transducers. The fifth stage using the Korobkin breakdown leads to fluid and bubble surface motion. Experiments on high speed droplet impact indicate that surface motion is independent of bubble or droplet size. In terms of the development of this theoretical fluid mechanical model we will ignore the compressible facets of jet impact and regard the impact as generating an impulsive fluid motion. Thus the potential on *both* sides of the 'cut', representing the impact site, will receive an impulse Π given by

$$\phi_a - \phi_b = -\frac{1}{\rho}\Pi, \tag{1}$$

where the potential ϕ_a is post- and ϕ_b is pre-impact. The impulse Π is given by

$$\Pi = \int p \, \mathrm{d}t. \tag{2}$$

However p is finite, and if we take the limit as the impact times goes to zero, then Π may be assumed to be zero. Thus the potential does not alter on impact for the purposes of this model. (Actually impact occurs at a point, having no area, so the force acting will be zero.) At the impact site the velocities will be equated and taken as an average of the pre-impact velocities as follows,

$$\frac{\partial \phi_u}{\partial n} = \frac{\partial \phi_e}{\partial n} = \frac{1}{2}\left[\frac{\partial \phi_e}{\partial n} + \frac{\partial \phi_u}{\partial n}\right]_{\mathrm{pre-impact}}, \tag{3}$$

where ϕ_u is the upper and ϕ_e, the lower surface potential at impact. The actual velocity after impact becomes the average velocity. Often, in practice, the liquid jet is moving at high speed, typically $\mathrm{O}(100\mathrm{ms}^{-1})$, while the other surface is near stationary.

Thus in taking a 'cut' across the jet impact site to form an additional surface we will have continuity in normal velocity but will be left with a jump $\Delta\phi$ in the potential, given by

$$\Gamma = \Delta\phi = \phi_u - \phi_e. \tag{4}$$

This potential corresponds to the circulation 'Γ' around the bubble and is the same for any circuit around the bubble. This assumption requires that we assume that no vortex sheet is generated, regarded by many as a contentious issue, and certainly in some circumstances a vortex sheet should be included.

After impact a toroidal bubble is formed although the impact stage is very difficult to observe even with very high speed cameras (upto 10^8fps). Ohl *et al.* (1999) has observed the detailed shock structure that occurs on jet impact and when the bubble is near to its minimum volume. As far as liquid motion is concerned, valuable information can be gained from liquid drop studies. Key questions are associated with the generation of vorticity and the formation of a splash. Typically jet velocities, V, are $\mathrm{O}(100\mathrm{ms}^{-1})$ while a typical jet diameter D for laser generated bubbles might be 0.2mm. This data gives values for the Weber and Froude number of

$$W_e = \left[\frac{\rho D V^2}{\sigma^2}\right]^{\frac{1}{2}} \sim 10^4, \qquad F_r = \frac{V}{(gD)^{\frac{1}{2}}} \sim 10^3, \tag{5}$$

where σ is the surface tension and g, gravitational acceleration. From the drop impact studies of Cresswell & Morton (1995) show that the formation of a vortex ring due to separation of a vortex sheet generated by a 'ring of contact' between the drop and liquid layer occurs when surface tension is important, typically for $W_e < 8$. In their studies they observed no vortex sheet being formed for an experiment when $W_e \approx 42$ and $F_r \approx 22$ but rather a splash and radial flow instead. These experimental studies therefore provide support for our neglect of a vortex sheet in our modelling and to concentrate on the propagating splash formation inside the bubble.

The next stage in the collapse of a bubble concerns the circumstances surrounding minimum volume (although jet impact can occur slightly after the bubble reaches minimum volume in some situations). The internal gas dynamics are modelled by assuming an ideal and adiabatic gas, given by the relation

$$p_e = p_v + p_0 \left(\frac{V_0}{V}\right)^{\kappa}, \tag{6}$$

where p_0 is the initial pressure, V_0, initial volume and κ is the ratio of specific heats. The temperature of the gas within the bubble is given by

$$T = T_a \left(\frac{V_a}{V}\right)^{\kappa - 1}, \tag{7}$$

where T_a is the ambient liquid temperature and V_a is the maximum bubble volume of the bubble during which time the gas equilibriates to the liquid temperature. Near minimum volume compressible effects can be important with radiation of acoustic energy and the formation of shock waves.

Finally the bubble rebounds returning to an incompressible flow behaviour but it is much less energetic with energy losses associated with acoustic radiation, shock waves, viscous dissipation, heat transfer and the resulting turbulent motion associated with liquid jet impact. It is likely that the most important factor will be energy losses associated with jet impact.

This section has briefly covered the key physical aspects associated with laser generated bubbles. A good starting position for modelling the fluid motion as being incompressible, irrotational and inviscid and to develop a computational technique that predicts the bubble shape, pressure, velocity throughout the growth, collapse and subsequent rebound of the bubble.

3 The Boundary Integral Method

In modelling the flow fields around vigorous pulsating bubbles near boundaries we assume that the flow field can be adequately modelled by an incompressible and inviscid liquid that is irrotational. This leads to the use of a velocity potential ϕ which allows us to develop an integral equation expression from the potential and unknown normal velocity $\partial\phi/\partial n$. Thus for a simply connected bubble with surface S we may write the integral equation as follows

$$c\left(\boldsymbol{p}\right)\phi\left(\boldsymbol{p}\right)=\int\limits_{S}\left\{G\left(\boldsymbol{p},\boldsymbol{q}\right)\frac{\partial\phi}{\partial n}\left(\boldsymbol{q}\right)-\phi\left(\boldsymbol{q}\right)\frac{\partial G}{\partial n}\left(\boldsymbol{p},\boldsymbol{q}\right)\right\}\mathrm{d}S, \tag{8}$$

where the Green's function $G(\boldsymbol{p},\boldsymbol{q})$ is given by

$$G(\boldsymbol{p},\boldsymbol{q})=\frac{1}{4\pi}\left(\frac{1}{|\boldsymbol{p}-\boldsymbol{q}|}+\frac{1}{|\boldsymbol{p}-\boldsymbol{q}'|}\right), \tag{9}$$

where $\boldsymbol{q}'$ is the position vector of the image of the point with position vector $\boldsymbol{q}$ in the rigid boundary. The normal $\boldsymbol{n}$ is taken to be directed into the interior of the bubble, and the coefficient $c(\boldsymbol{p})$ is $1/2$ if $\boldsymbol{p}\in S$ and 1 if $\boldsymbol{p}$ is the position vector of a point elsewhere in the fluid.

The essence of the approach is that initially either a specified potential is given on the surface of the bubble or an initial pressure (with zero potential) inside the bubble or a combination of both is provided.

The first kind Fredholm equation for $\partial\phi/\partial n$ given in (8) is solved computationally following earlier approaches outlined in Blake, Taib & Doherty (1986), Best (1993) and Tong *et al.* (1999). With a knowledge of $\partial\phi/\partial n$ and ϕ on the bubble surface we may then update the position of given Lagrangian values that are used to define the surface. The potential ϕ may also be updated by exploiting the dynamic conditions on the bubble surface which yields the following,

$$\frac{\mathrm{d}\phi}{\mathrm{d}t}=1+\frac{1}{2}\left|\nabla\phi\right|^{2}-\alpha\left(\frac{V_0}{V}\right)^{\kappa}-\delta^{2}(z-\gamma)+\frac{K}{\mathrm{We}}. \tag{10}$$

In (10) the following dimensionless qualities have been defined: compression ratio, $\alpha=p_0/\Delta p$; buoyancy parameter, $\delta^2=\rho g R_{\mathrm{m}}/\Delta p$ and Weber number $W_e=R_{\mathrm{m}}\Delta p/\sigma$. Here, p_0 is the initial pressure inside the bubble due to the non-condensible part of the gaseous contents of the bubble, g is the gravitational acceleration, ρ is the fluid density, R_m is the maximum bubble radius, V_0, the initial bubble volume at time t, σ, the surface tension and K, the curvature. The quantity $\Delta p=p_\infty-p_v$, where p_∞ is the ambient pressure at the bubble location and p_v is the vapour pressure. A further important dimensionless parameter is the standoff parameter, γ, defined as follows

$$\gamma=\frac{h}{R_m}, \tag{11}$$

where h is the distance that the bubble is from the boundary on initiation.

In some circumstances the bubble may collapse asymmetrically, developing a high speed liquid jet which may thread the bubble completely leading to a toroidal bubble. This creates a problem because the bubble is now doubly connected. Best (1993,94) overcame this difficulty be creating a 'cut', T, across the jet to

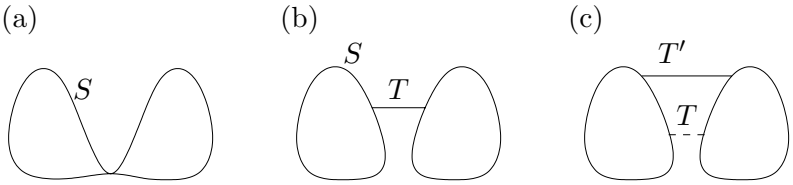

Figure 2: Schematic representation of the transition to a toroidal geometry: (a) just prior to jet impact, (b) following jet impact with the addition of a cut T, and (c) dynamic cut relocation from T to T'.

once again produce a simply connected domain. Based on earlier discussions in Section 2, a new boundary integral formulation is obtained,

$$c(\boldsymbol{p})\phi(\boldsymbol{p}) = \int\limits_{S\setminus T} \left\{ G\left(\boldsymbol{p},\boldsymbol{q}\right) \frac{\partial \phi}{\partial n}\left(\boldsymbol{q}\right) - \phi\left(\boldsymbol{q}\right) \frac{\partial G}{\partial n}\left(\boldsymbol{p},\boldsymbol{q}\right) \right\} \mathrm{d}S - \Delta\phi \int\limits_{T_+} \frac{\partial G}{\partial n}\left(\boldsymbol{p},\boldsymbol{q}\right) \mathrm{d}S. \tag{12}$$

This formulation accounts for the circulation $\Delta\phi$ around the bubble. Further details can be found in Best (1993).

4 Computational Results

In Figures 3–8 graphical output from a range of example calculations for a laser-generated bubble near a rigid boundary, a free surface and in a shallow layer of liquid. With the exception of two cases, all the results show the interesting features associated with toroidal bubble behaviour.

Figure 3 shows the pressure contours and velocity vectors associated with a cavitation bubble near a rigid boundary both prior to and following liquid jet impact. Features to note are the high pressures above the bubble before jet impact, the high relative velocities in the jet, and the high pressure on the rigid boundary after impact. The influence of the standoff distance and compression ratio is shown in Figures 4 and 5. The case of most interest is that shown in Figure 4(b) where jet impact occurs during rebound. In Figure 5(a) a 'splash' inside the bubble is clearly evident. The bubble shapes shown in Figures 4(a) and 5(b) are very similar to experimental observations. Figure 6(a) shows the interesting feature of the existence of a maximum jet speed at a given standoff distance (γ) for each compression ratio (α). One of the ramifications of this observation is that for $\gamma > \gamma_c$ the liquid jet does not impact on the far-side of the bubble because the bubble wall rebounds faster. In Figure 6(b) the temperature is calculated using (7). The lower temperatures at small γ are associated with kinetic energy being tied up with the ring vortex and not being available for bubble compression.

Figure 7 shows the behaviour of bubbles at different standoff distances from a free surface. In each case the jet is directed away from the free surface with the jet becoming wider for larger standoff distances. Figure 8 illustrates bubble behavior in a thin fluid layer with potential applications to laser surgery in the eye or in other shallow layers such as tissue.

5 Conclusions

The boundary integral method has proved to be a highly accurate computational technique for modelling the fluid mechanics of the first few pulsations of a laser generated bubble near boundaries when inertial forces predominate over dissipative effects such as viscosity and compressibility. Calculations appear to accurately reproduce a range of experimental results recorded with very high speed cameras (now up to 100 million frames per second!) as well as providing further insight into the physics of fluid behaviour by calculating bubble shape, velocity vectors and pressure fields. The calculations in particular show the shape and speed of liquid jets and splashes, the pressure field, in particular the sites of intense pressure that could lead to mechanical defects as well as the likely location for shock formation.

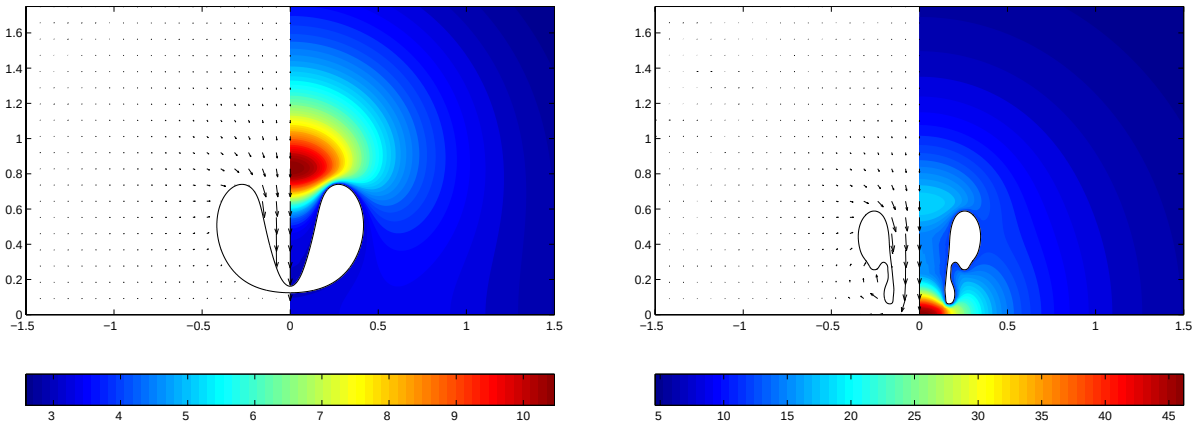

(a) Just prior to liquid jet impact, time 2.223.

(b) Following liquid jet impact, time 2.274.

Figure 3: Velocity vectors and pressure contours for the case $\alpha = 100$, $\gamma = 1.1$.

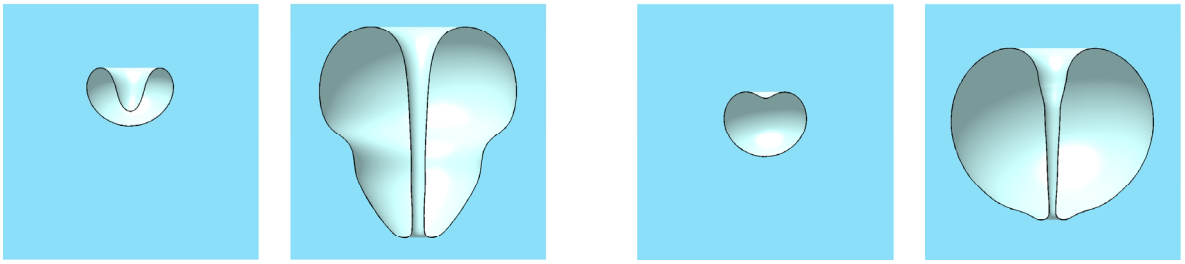

(a) $\gamma = 3$. Times are 2.0699 and 2.1608.

(b) $\gamma = 5$. Times are 2.0202 and 2.0675.

Figure 4: Half rendered bubble shapes for $\alpha = 100$. The left-hand frame of each pair shows the bubble at minimum volume. The right-hand frame shows motion at a later time during the rebound phase on the same axes.

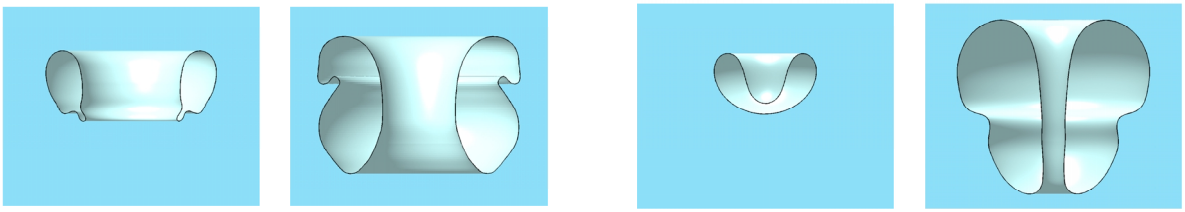

(a) $\gamma = 3$. Times are 1.9962 and 1.9976.

(b) $\gamma = 5$. Times are 1.9436 and 1.9527.

Figure 5: Half rendered bubble shapes for $\alpha = 1000$. The left-hand frame of each pair shows the bubble at minimum volume. The right-hand frame shows motion at a later time during the rebound phase on the same axes.

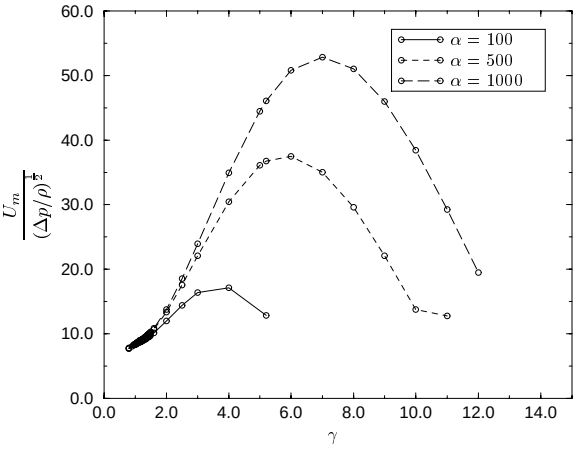

(a) Maximum jet velocity against dimensionless standoff for 3 compression ratios $\alpha = 100, 500$ and 1000. If we suppose that Δp is approximately one atmosphere then $\sqrt{\Delta p/\rho} = 10\text{ms}^{-1}$.

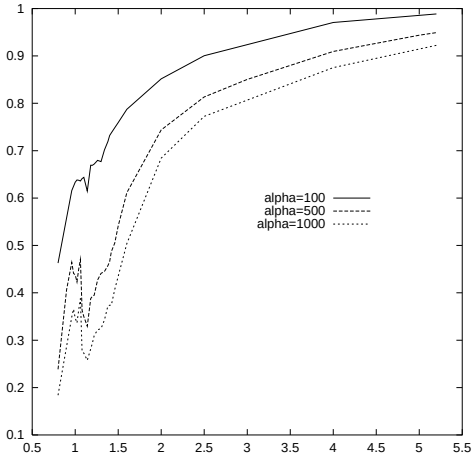

(b) Dimensionless maximum temperature (during later stages of motion) versus dimensionless standoff, $\alpha = 100$, 500 and 1000.

Figure 6: Jet velocities and temperatures as a function of standoff distance.

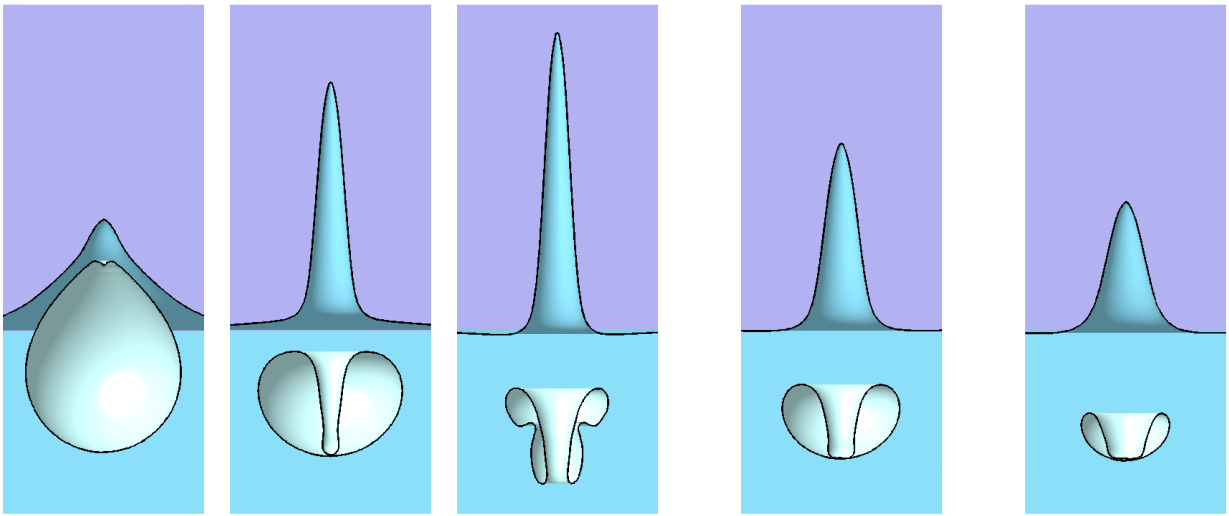

(a) $\gamma = -0.56$. Times are 0.4476, 1.0471 and 1.2749.

(b) $\gamma = -0.7$. Time is 1.2742.

(c) $\gamma = -0.85$. Time is 1.4232.

Figure 7: Half rendered shapes for vapour bubble motion near a free surface for a range of standoff distances.

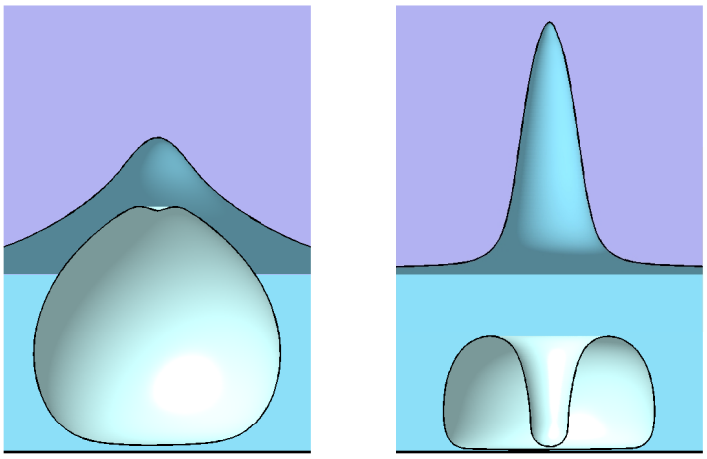

Figure 8: Half rendered bubble and surface shapes for the motion of a cavitation bubble in a shallow layer of fluid for the case $\alpha = 100$, $\gamma_{RB} = 0.7$ and $\gamma_{FS} = -0.7$ (i.e. $D = 1.4$). Times are 0.6577 and 1.2891.

References

Best, J. P. 1993 The formation of toroidal bubbles upon the collapse of transient cavities. *J. Fluid Mech.* **251**, 79–107.

Best, J. P. 1994 *The rebound of toroidal bubbles.* In: Bubble dynamics and interface phenomena. Eds. J. R. Blake, J. M. Boulton-Stone & N. H. Thomas. Kluwer, Dordrecht, pp. 405–412.

Blake, J. R. & Keen, G. S. 1998 *Theoretical developments in acoustic cavitation.* 3rd Biennial Engineering Mathematics Conference, Adelaide, pp. 131–134.

Blake, J. R., Taib, B. B. & Doherty, G. 1986 Transient cavities near boundaries. Part 1. Rigid boundary. *J. Fluid Mech.* **170**, 479–497.

Blake, J. R., Taib, B. B. & Doherty, G. 1987 Transient cavities near boundaries. Part 2. Free surface. *J. Fluid Mech.* **181**, 197–212.

Cresswell, R. W. & Morton, B. R. 1995 Drop-formed vortex rings - the generation of vorticity. *Phys. Fluids* **7**, 1363–1370.

Guerri, L., Lucca, G. & Prosperetti, A. 1981 A numerical method for the dynamics of non-spherical cavitation bubbles. *Proc. of the 2nd International Colloquium on Drops and Bubbles,* pp. 175–181.

Korobkin, A. A. 1997 Asymptotic theory of liquid-solid impact. *Phil. Trans. Roy. Soc.* **A355**, 507–522.

Ohl, C. D., Mettin, R., Luther, S., Lindau, O. & Lauterborn, W. 1999 Bubble dynamics, shock waves and sonoluminescence. *Phil. Trans. Roy. Soc.* **A357**, 269–294.

Prosperetti, A. & Lezzi, A. 1986 Bubble dynamics in a compressible liquid. Part 1. First order theory. *J. Fluid Mech.* **168**, 457–478.

Tong, R. P., Schiffers, W. P., Shaw, S. J., Blake, J. R. & Emmony, D. C. 1999 The role of 'splashing' in the collapse of a laser generated cavity near a rigid boundary. *J. Fluid Mech.* **380**, 339–361.